ACS OMEGA

Article

Cite This: ACS Omega 2019, 4, 19934−19943

http://pubs.acs.org/journal/acsodf

# Multiscale Characterization of a Wood-Based Biocrude as a Green Compatibilizing Agent for High-Impact Polystyrene/Halloysite Nanotube Nanocomposites

Bjarke Høgsaa,[†] Thomas H. Pedersen,[†] Masoumeh Mousavi,[‡] Albert M. Hung,[‡] Erik Appel Jensen,[§] Donghong Yu,[†] Jesper de Claville Christiansen,[†] Catalina-Gabriela Sanporean,[†] and Elham H. Fini*[,‡]

[†]Aalborg University of Denmark, Aalborg East, Aalborg 9220, Denmark

[‡]Arizona State University, 660 S. College Avenue, Tempe, Arizona 85287-3005, United States

[§]Aarhus University School of Engineering, Birk centerpark 15, Herning 7400, Denmark

Supporting Information

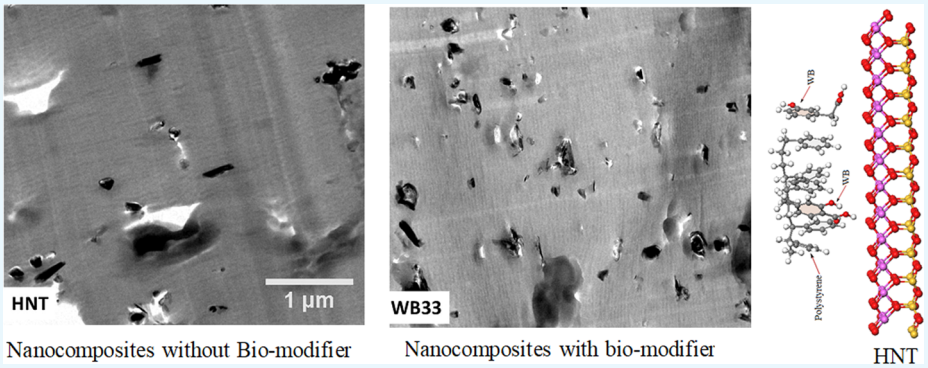


**ABSTRACT:** This paper investigates merits of using a wood-based biocrude (WB) from aspen wood to improve the compatibility of halloysite nanotubes (HNTs) with high-impact polystyrene to develop nanocomposites with desirable thermomechanical properties. Morphological, thermal, and rheological properties of the resulting nanocomposite are used as indicators of the compatibility and dispersion of the modified HNT within the polymer matrix. Computational modeling using density functional theory is used along with laboratory experiments to provide a multiscale characterization of the above biocrude and nanocomposites. Studies performed through dispersion-corrected density functional theory calculations show that the active functional groups of WB molecules including carbonyl, hydroxyl, and carboxylic interact with the HNT surface, while their aromatic tails interact with the phenyl groups of the polystyrene. Furthermore, the studies reveal how WB molecules act as bridges between the hydrophobic polymer and the hydrophilic clay improving the compatibility. The latter was confirmed by Hansen solubility parameters and was evidenced in improved dispersion of clay within the polystyrene matrix observed by microscopy. Rheological and thermal analyses of the modified HNT and nanocomposites showed physical interactions of WB with HNT surface as well as interactions between the WB-modified HNT and the high-impact polystyrene. The WB was found to be a strong candidate as a green compatibilizing agent for HNT in high-impact polystyrene. The study results can provide insights for formulators and manufacturers looking for green compatibilizing agents in conventional nanocomposites for construction and manufacturing applications.

## 1. INTRODUCTION

Nanocomposites with improved thermal, rheological, and mechanical properties have been a focus of research, especially due to the recent development of novel surface-modified nanofillers.[1,2] Halloysite nanotubes (HNTs) are low-cost, environmentally friendly, and readily available nanofillers with a chemical structure similar to that of kaolinite, except that the structure is rolled into a hollow tube instead of a sheet. HNTs have a molecular formula of $Al_2Si_2O_5(OH)_4{\cdot}nH_2O$. The external surface is composed of siloxane (−Si−O−Si−), and the internal surface is aluminol (−Al−OH).[3−6] The tubular structure and external siloxane surface with few OH groups improve the natural dispersion of HNT.[5] However, due to the negatively charged external surface, HNTs typically have poor compatibility with some hydrophobic polymers. Surface modification via van der Waals forces, hydrogen bonding, and electrostatic attractions can improve the compatibility issue.[7] Previous studies have shown that pure HNT without modification will agglomerate when mixed with hydrophobic

Received: September 4, 2019
Accepted: October 31, 2019
Published: November 14, 2019

polymers, which negatively affects the thermal and mechanical properties of the mixture.[8]

High-impact polystyrene (HiPS) is an important thermoplastic polymer that is extensively used in products in fields such as transportation, electronic packaging, automobiles, and household appliances.[9,10] HiPS is an immiscible, phase-separated polymer blend with major polystyrene (PS) and minor polybutadiene (PBD) phases; most commercial HiPSs have about 4−12% PBD.[11] The introduction of nanofillers such as HNT in the polymer to enhance its properties has been regularly practiced.[3−6] However, the compatibility between HNT and the polymer (HiPS) is a concern due to the hydrophilic nature of the clay, although different types of modifiers have been introduced to enhance the compatibility of HNT and HiPS.[12,13]

In this study, a wood-based biocrude (WB) is used as a new modifier acting as a bridge between HNT and HiPS. The specific hypothesis is that the compatibility of HNT and HiPS will be improved when a biocompatiblizing agent is used. This in turn enhances the sustainability of conventional nanocomposites.

## 2. RESULTS AND DISCUSSION

**2.1. Structures and Morphologies of the Pure and WB-Modified HNTs.** *2.1.1. X-ray Diffraction (XRD).* The diffraction patterns of the nanoclays are shown in Figure 1. It

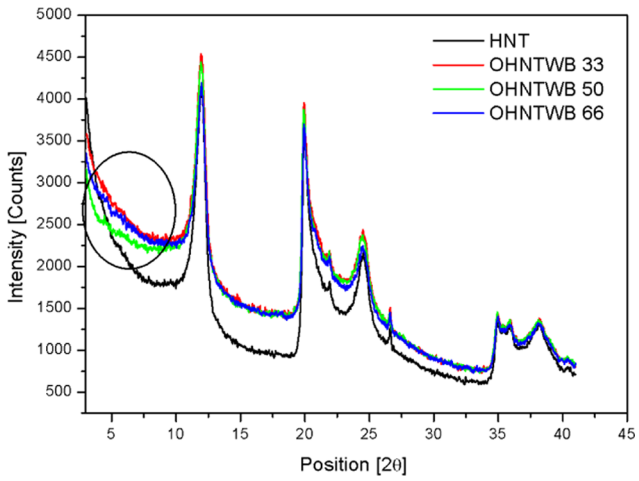


**Figure 1.** XRD analysis of the pure HNT and WB-modified HNTs.

can be observed that the diffraction patterns of modified nanoclays were almost identical to those of the raw HNT, except at around 3−8° 2$\theta$. No peaks in this area were present for the OHNTWB 33, while the OHNTWB 50 and OHNTWB 66 have two broad peaks at 5.43−5.61 and 4.33−4.39°, respectively. This could indicate better dispersion and less agglomeration of the OHNTWB 33 compared to the OHNTWB 50 and OHNTWB 66. The unchanged diffraction patterns of the modified halloysite nanoclays indicate that modification did not change the interior lumen of the HNTs. This result could mean that either grafting of the WB occurred only on the outer silica surface or the WB entered only the interior lumens without unraveling the tubular structure of the HNT. Similar results of both scenarios are reported in other studies.[14,15]

*2.1.2. Dynamic Light Scattering (DLS).* Results of the DLS measurements of the pure and modified nanoclays are listed in Table 1. A reduction in the average particle size of modified nanoclays was observed with an increasing amount of WB. The

**Table 1. Particle Size and $\zeta$-Potential of the Pure and WB-Modified HNTs Measured by DLS**

| sample | average particle size [$d$, nm] | average $\zeta$-potential [mV] | average polydispersity |
|---|---|---|---|
| HNT | 440 | −0.64 | 0.20 |
| OHNTWB 33 | 347 | −5.49 | 0.23 |
| OHNTWB 50 | 351 | 0.46 | 0.27 |
| OHNTWB 66 | 282 | −1.78 | 0.15 |

typical dimensions of the nanotubes are in the range of 0.1−15 $\mu$m, with an inner diameter of 5−30 nm and an outer diameter of 30−70 nm.[16] The decrease in average particle size can be interpreted as a sign of de-agglomeration and enhanced dispersion.[17,18] It can be seen that the introduction of WB reduced the average particle size from that of pure HNT ($d$, 440 nm) to 347, 351, and 282 as the concentration of WB increased. Also, the polydispersity was the lowest for the sample with the highest WB dosage, indicating a narrower and more uniform distribution of the particles associated with reduced agglomerations. Although the scenario with the highest concentration of WB (OHNTWB 66) showed the smallest average particle size, this scenario was not the most stable. In fact, OHNTWB 33 showed the highest stability, as evidenced by the largest $\zeta$-potential of −5.49, which indicates the strongest electrostatic charges giving rise to repulsion forces and preventing agglomeration.

*2.1.3. Attenuated Total Reflectance Fourier Transform Infrared (ATR-FTIR) Spectroscopy.* The FTIR analysis of the pure and modified HNTs (Figure 2) shows that the HNTs exhibit characteristic absorption bands near 1092, 1030, and 910 $cm^{-1}$ that are associated with the stretching vibration of Si−O bonds and flexural vibrations of Al−OH.[19] The stretching vibrations at 3695 $cm^{-1}$ associated with the inner surface OH groups and the stretching bands at 3622 $cm^{-1}$ of the inner Al−OH groups are present in all nanoclays. The bands at around 3650 and 3670 $cm^{-1}$ (Figure 2A, black circle) are the characteristic of the opening and modification of the HNT lumen,[3,14,20−22] although the peaks are very small.

In Figure 2B, the peak at 940 $cm^{-1}$ is associated with the OH deformation of the inner surface hydroxyl group. This peak becomes more visible with increasing dosages of WB. The peak at 912 $cm^{-1}$ is associated with the OH deformation of inner hydroxyl groups; this peak shifts toward higher wavelengths with increasing dosages of WB. A peak for the in-plane Si−O stretching at 1070 $cm^{-1}$ shifts toward higher wavelengths and becomes more visible with increasing dosages of WB.

The results of the analyses of the morphologies and structures of the modified nanoclays indicate that several compounds of the WB have been grafted on the outer surface and small amounts could have entered the interior lumen of the HNT.

**2.2. Thermal Properties of the Pure and WB-Modified HNTs.** The increase in WB concentration among the three samples leads to a reduction in the thermal resistance of the nanocomposites. The three modified nanoclays show very similar thermal resistance, with OHNTWB 66 showing a small



DOI: 10.1021/acsomega.9b02871
ACS Omega 2019, 4, 19934−19943

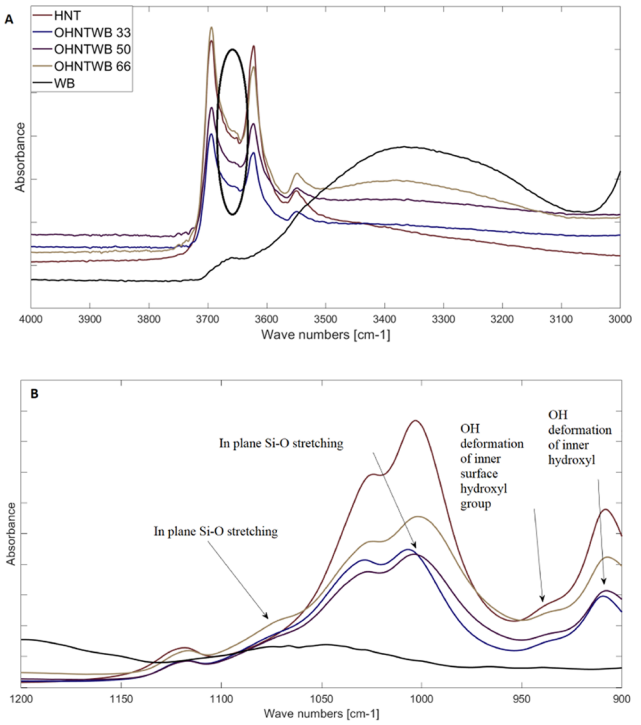


**Figure 2.** FTIR analysis of pure WB, pure HNT, and the WB-modified HNT clays in the (A) 3000−4000 $cm^{-1}$ range and (B) 900−1200 $cm^{-1}$ range.

drop of 1% mass loss at around 200 °C, indicating that at a high concentration of WB, some excess biocrude may be trapped inside the halloysite nanotubes, contributing to a slight loss of mass (Table 2).

**Table 2. TG Analysis of the WB, HNT, and WB-Modified HNTs**

| | temperature range <1000 °C | |
|---|---|---|
| | [°C] | mass loss [%] |
| WB | 146.0 | 87.0 |
| HNT | 449.4 | 17.3 |
| OHNTWB 33 | 139.2 | 42.5 |
| OHNTWB 50 | 139.7 | 43.7 |
| OHNTWB 66 | 139.7 | 43.9 |

Despite the differences in WB concentration, the mass loss is nearly the same at all registered processing temperatures (Table 3); it could be concluded that only the excess WB is removed from the exterior surfaces of the HNT, and the remaining residual masses contain primarily HNT with bonded compatibilizer molecules. Other studies have found that an increase in the WB concentration decreased the loss of organic residue in the range 100−300 °C from evaporation or decomposition of the molecules of the modifier; this study also found that result, but the decreases in modified clay in these regions were small in comparison with those of the other studies.[7,23]

The changes in the structure and morphologies of the modified OHNT compared to those of the pure HNT show that organic modification and grafting of WB were successful.

**2.3. Hansen Solubility Parameter (HSP) Analysis of the Interaction between WB Compounds and Polystyrene.** Hansen solubility parameters (HSPs) can be used as a preliminary compatibility assessment tool to test whether a polymer is soluble and compatible with intercalant compounds.[24] The solubility hypothesis assumes that a surface-treated nanoparticle will be compatible with a polymer if the backbone of the molecules on the nanoparticle surface is a solvent for the polymer. Table S1 (Supporting Information) lists the calculated values of the relative energy difference (RED) between the known components in WB and PS; PS is the closest polymer analogue available for HiPS. The fractional HSP values plotted in Figure 3 suggest that the WB ketone

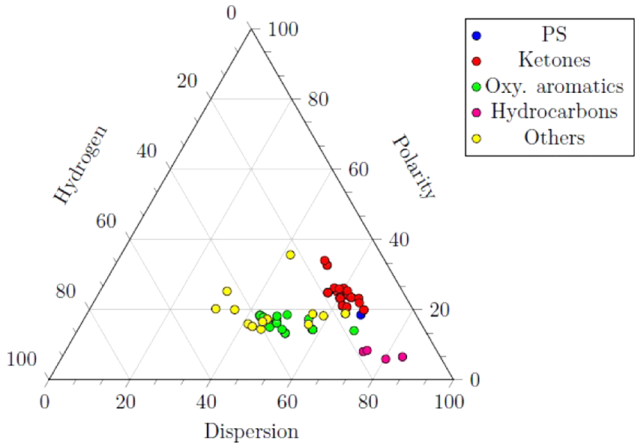


**Figure 3.** Teas chart showing the fractional HSP values of PS and WB compounds.

compounds are the most compatible with PS. However, the PS also matches with some other oxygenated aromatics in the WB, which was described by Pedersen and co-workers.[25] This information suggests that the aromatic groups of PS are the most compatible with selected compounds of the WB.

**2.4. Molecular Modeling.** In this section, we show how biomodification using wood-based crude oil can increase the compatibility of halloysite nanoclay with polystyrene (PS). Fractional HSP values (Figure 3) show that the oxygenated

**Table 3. TG Analyses of the Mass Losses and Residual Masses at 80, 230, 600, and 1000 °C of the Pure and WB-Modified HNTs**

| | mass losses and residual masses at 80, 230, 600, and 1000 °C | | | | | | | |
|---|---|---|---|---|---|---|---|---|
| | $M_{80}$ [%] | $R_{80}$ [%] | $M_{230}$ [%] | $R_{230}$ [%] | $M_{600}$ [%] | $R_{600}$ [%] | $M_{1000}$ [%] | $R_{1000}$ [%] |
| WB | 5.7 | 94.3 | 50.8 | 49.2 | 83.5 | 16.5 | 87.0 | 13.0 |
| HNT | 0.8 | 99.2 | 1.2 | 98.8 | 12.8 | 87.2 | 17.3 | 82.7 |
| OHNTWB 33 | 0.7 | 99.3 | 14.9 | 85.1 | 41.2 | 58.8 | 42.5 | 57.5 |
| OHNTWB 50 | 0.9 | 99.1 | 15.2 | 84.8 | 41.2 | 58.8 | 43.7 | 56.3 |
| OHNTWB 66 | 0.6 | 99.4 | 16.6 | 83.4 | 42.8 | 57.2 | 43.9 | 56.1 |



DOI: 10.1021/acsomega.9b02871
ACS Omega 2019, 4, 19934−19943

aromatics and ketones of WB are most compatible with PS; therefore, we use these molecules as model compounds to study the bridging role of WB between HNT and PS. It should be noted that the adsorption of the organic molecules (PS and WB) mainly occurs on the outer surface of the HNT containing O−Si−O groups. The inner surface of HNT containing Al−OH groups has limited space, and its active sites are not as accessible as those on the outer layer.

The PS model compound contains five repeating units from the polymer molecule. Since each WB molecule has a chance to interact with just a small part of the polymer, and the interaction between the polymer and the HNT surface is defined as interaction per surface area, this model properly describes the interacting constituents in the system.

Depending on the arrangement of the pendent (phenyl) groups along the backbone chain of the polymer, three tacticities are defined for the polystyrene: isotactic, where the phenyl groups are arranged on one side of the polymer; syndiotactic, where phenyl groups are hanging from alternating sides of the polymer backbone chain; and atactic, where phenyl groups are randomly arranged. Based on dispersion-corrected density functional theory (DFT-D) at the BPE/DNP level using DMol$^3$, our calculations show that the syndiotactic arrangement for the PS model compound is more stable than that of its counterpart with the isotactic arrangement by 19.7 kcal/mol (Figure 7). In practice, the higher thermodynamic stability of syndiotactic PS compared to isotactic PS manifests itself in higher crystallization rate (2 orders of magnitude) and higher melting point of syndiotactic PS (275 °C) compared to the isotactic PS (240 °C).[26] Therefore, the syndiotactic conformer was chosen as the PS model in this study. Figure 4 shows that the carbon atoms of the optimized structures of isotactic or syndiotactic are not in a straight or zigzag link.

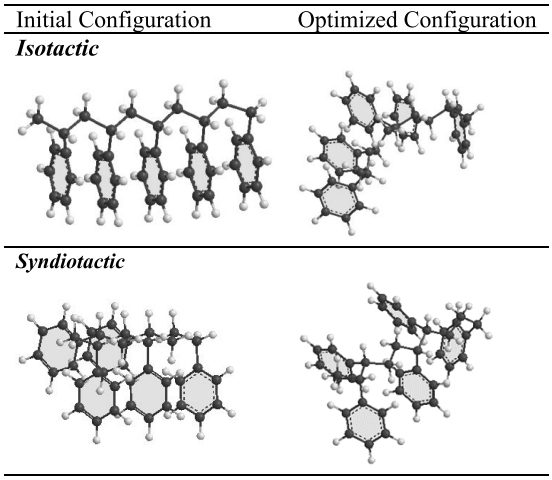


**Figure 4.** Initial and fully optimized conformers of the PS model employed in this study. Based on the DFT-D calculations at the BPE/DNP level, the syndiotactic configuration is thermodynamically more stable than the isotactic configuration by 19.7 kcal/mol.

It has been documented that when the surface of montmorillonite clay is treated with a particular biomodifier, an organophilic environment is created around the clay that improves the hydrophobic nature of the polymer, causing the polymer to be adsorbed onto the clay.[27,28] In other words, molecules of the compatibilizer act as a bridge between the hydrophobic polymer and the hydrophilic clay (Figure 5).

Components identified in aspen wood include functional groups such as carbonyl (C═O), hydroxyl (OH), carboxylic (COOH), and phenyl groups. It is not expected that these polar groups would be attracted to silicon oxide groups of the HNT surface through electrostatic and van der Waals forces such as H-bonding and dipole−dipole interactions. The components of WB are attached to the HNT surface by their active functional groups from one side and to the polymer by their aromatic tail from the other side. However, the main question raised is how the inactive tails of WB molecules interact with the rather bulky pendent (phenyl) groups of the PS that are hanging from the polymer backbone chain. To answer this question, we will focus on the interaction mechanism between polystyrene and WB molecules.

Table 4 shows the results of the DFT-based molecular modeling for interaction between some selected WB molecules and phenyl groups of the PS. WB molecules chosen in this molecular modeling are among the oxygenated aromatics and ketones that are found in abundance in aspen wood. The extended transition state−natural orbital of chemical valence (ETS-NOCV) technique was used to decompose the total binding energy between two fragments into its components: electrostatic interaction ($\Delta E_{elstat}$), Pauli repulsion ($\Delta E_{Pauli}$), orbital interaction ($\Delta E_{orb}$), and dispersion ($\Delta E_{disp}$) energies (Table 4).

In the aromatic group, the electrostatic and dispersion interactions contribute significantly to the total binding energy (see $\Delta E_{elstat}$ and $\Delta E_{disp}$, respectively). This could be due to the electrostatic interactions between aromaticities of the face-to-face phenyl rings. Almost all energy components related to the aromatic group show higher values compared to their counterparts in nonaromatic cyclic ketones, indicating the significance of oxygenated aromatics in establishing an appropriate overlap between $\pi$ densities of WB and PS fragments.

It should be further noted that although the aromatic components of WB benefit from the $\pi-\pi$ interaction with phenyl groups of the PS, their interaction energy is not much higher than that of cyclic nonaromatic ketones. It was found that a part of this energy is coming from the $\pi$−H interactions between the $\pi$ electronic density of the PS phenyl rings and H of the cyclic nonaromatic compounds of WB. Additionally, in the case of 2-cyclopenten-1-one, 3,4-dimethyl, shown in Table 4, $\pi$ conjugated orbitals of the WB molecule use their ability to overlap with $\pi$ orbitals of the PS polymer. Therefore, the energy terms shown in Table 4 verify the effective binding interactions between special compounds of WB and the PS polymer.

**2.5. Rheological Properties of the OHNT/HiPS Nanocomposites.** The rheological analysis of the HiPS nanocomposites shown in Figure 6 confirms the interactions between modified nanoclay and the polymer matrix, which, in turn, supports the findings of the HSP and molecular modeling. The observed interactions are evidenced by a deviation from the low-frequency plateau, indicating the formation of a soft solid in the HiPS nanocomposite mixed with OHNTWB 33. These formations are related to improved thermal and mechanical properties of the resulting nanocomposite, due to the better compatibility and dispersion of the nanoclays with the polymer matrix.[9,28−30] However, such an interaction was not observed with an increased amount of WB, as the HiPS OHNTWB 50 and 66 nanocomposites did not show soft-solid formation. This could be due to a thicker


DOI: 10.1021/acsomega.9b02871
ACS Omega 2019, 4, 19934−19943

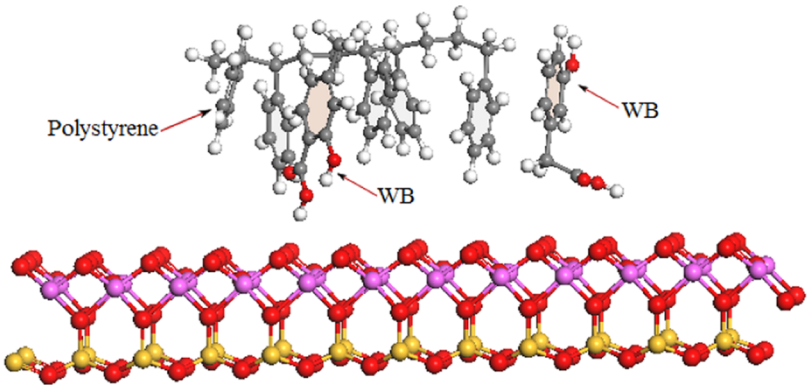


**Figure 5.** Interaction of the polystyrene model molecule with the surface of halloysite nanotubes in the presence of the selected molecules of wood-based biomodifier (WB).

surfactant layer that increases the molecular spacing between the clay and polymer while also reducing the electrostatic charge of the clay surface. This thicker surfactant layer could be the result of inadequate mixing or excess compatibilizer after surface modification. Another possible explanation for the reduced interaction and viscosity could be the release of stored WB from inside the HNTs. This excess compatibilizer could reduce the interaction between the polymer and HNT, or it could soften the matrix by dissolving into the polymer.

The reduced complex viscosity at high frequencies for the HiPS-HNT composite compared to the pure polymer indicates that there is particle-induced viscosity reduction. This phenomenon was first reported by Mackay and co-workers,[31] where a relatively small amount of nanoparticles can lead to a significant particle-induced reduction in viscosity compared to the viscosity of the polymer matrix. The reduction is due to the clay agglomerating and producing flocculated structures that have a fractal influence on the viscosity via an increase in apparent volume. This can be explained by the Kriger–Dougherty-modified Einstein equation for the influence of packing fraction on viscosity for filled systems.[32] The agglomerated structure of the HNT is evidenced by DLS measurements showing the largest particle size and a low $\zeta$-potential for the pure HNT. The WB-grafted HNTs achieved a better dispersion within the HiPS matrix, which could lead to improved properties of the nanocomposites.

**2.6. Structures and Morphologies of the OHNT/HiPS Nanocomposites.** *2.6.1. TEM.* TEM images of the HiPS nanocomposites reveal that the nanotubes were most thoroughly dispersed in the OHNTWB 33 nanocomposite (Figure 7). The enhanced dispersion is attributed to the presence of high electrostatic forces in this scenario, as evidenced by the $\zeta$-potential. Such an enhancement is also reflected in the rheological properties showing a significant enhancement of the viscosity for this specific nanocomposite. In addition, large nanotube aggregates were regularly found in each of the nanocomposite formulations, except for HiPS OHNTWB 33 (see Figure S1, Supporting Information). The nanotubes often appeared hollow or collapsed rather than filled or exfoliated; however, the structure of individual nanotubes did not show noticeable differences among the three nanocomposites (Figure S2, Supporting Information).

*2.6.2. ATR-FTIR.* The FTIR analysis of the nanocomposites in Figure 8 shows the appearance of a broad peak (I) due to polar compounds (e.g., alcohols or carboxylic acids) present in the nanocomposites with the lowest amounts of WB (33 and 50%) in the modified nanoclays.

Specific peaks, as indicated with arrows in Figure 8B, were found in the II range. The OH deformation of water from HNT was found at 1650 $cm^{-1}$, but it increases in intensity and shifts. Three peaks appear in the nanocomposites that are specifically related to the modified nanoclay: a peak from WB ketones at 1716 $cm^{-1}$, a peak at 1470 $cm^{-1}$ associated with deformation (scissoring) of $CH_2$, and a peak at 1120 $cm^{-1}$ from perpendicular Si–O stretching from HNTs. These peaks increase and shift in composites.[12,33]

However, the HiPS/OHNT/WB 33 presented a new peak at 1045 $cm^{-1}$ that is associated with Si–O–C.[34] This may indicate a strong bonding between the nanoclay and either WB compounds or HiPS that developed during blending. Such bonding would also further explain the interaction between modified OHNTWB 33 and the HiPS that is observed in the rheological results.

The results of the rheological and analyses of the structures and morphologies of the OHNT/HiPS demonstrated that interactions between the OHNTs and HiPS were achieved.

**2.7. Thermal Properties of the OHNT/HiPS Nanocomposites.** Thermogravimetric analysis of the HiPS nanocomposites showed that the composites undergo one primary thermal decomposition stage at about 410–420° (Table 5). The addition of WB slightly increases the decomposition temperatures of nanocomposites. These results align with those of prior studies.[12,35] The HiPS nanocomposites showed improved thermal resistance with an increasing dosage of WB. This may be attributed to the improved dispersion and compatibility of clay in the polymer.

## 3. CONCLUSIONS

The paper investigated the merits of using wood-based biocrude (WB) produced from biorenewable and sustainable resources such as aspen wood, as a modifier for halloysite nanotubes (HNTs) to improve the compatibility of HNT with polymeric matrixes. A nanocomposite with the biomodified HNT and high-impact polystyrene was produced. Hansen solubility parameters combined with molecular modeling showed that WB's ketone compounds and oxygenated aromatics are compatible with polystyrene. Molecular modeling and morphological analyses show that functional groups of the WB including carbonyl, hydroxyl, and carboxylic activate the HNT surface, while the aromatic tail of these molecules establishes bonding interactions with phenyl groups of the



DOI: 10.1021/acsomega.9b02871
ACS Omega 2019, 4, 19934–19943

**Table 4. Energy Decomposition Results, at the BPE-D3/DZP Level, for the Interaction of the Polystyrene Model and Some Selected Components of Wood-Derived Biocrude (WB) Belonging to the Oxygenated Aromatic and Ketone Categories[a]**

| WB molecule | Polystyrene + WB molecule | $\Delta E_{Pauli}$ | $\Delta E_{elstat}$ | $\Delta E_{orb}$ | $\Delta E_{disp}$ | $\Delta E_{total}$ |
|---|---|---|---|---|---|---|
| ***Oxygenated Aromatics*** | | | | | | |
| 4-Hydroxyphenethyl alcohol 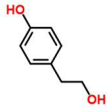 | 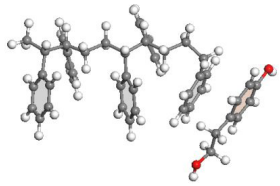 | 14.91 | -12.63 | -6.49 | -8.27 | -12.47 |
| 2-Hydroxy-4-methylbenzoic acid 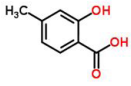 | 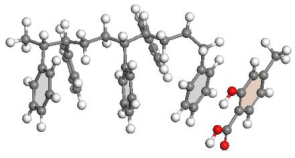 | 15.58 | -14.30 | -6.50 | -8.39 | -13.65 |
| 4-Methylcatechol  | 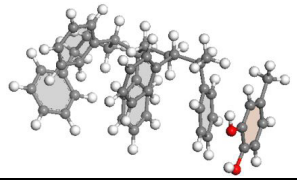 | 13.87 | -10.81 | -6.42 | -7.62 | -11.08 |
| ***Cyclic Ketones*** | | | | | | |
| WB molecule | Polystyrene + WB molecule | $\Delta E_{Pauli}$ | $\Delta E_{elstat}$ | $\Delta E_{orb}$ | $\Delta E_{disp}$ | $\Delta E_{total}$ |
| Cyclohexanone, 2-ethyl  | 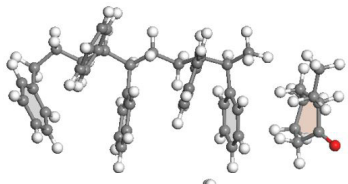 | 10.64 | -8.71 | -6.10 | -6.91 | -11.70 |
| 2-Cyclopenten-1-one, 3,4-dimethyl 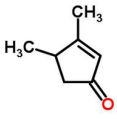 | 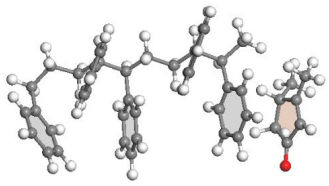 | 16.09 | -11.98 | -6.90 | -7.83 | -10.63 |
| Cyclopentanone, 2-methyl 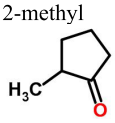 | 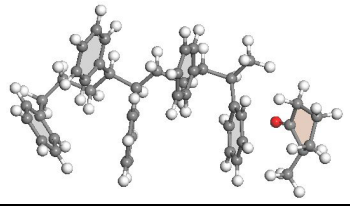 | 9.82 | -8.65 | -5.76 | -6.13 | -10.73 |

[a]All energies are in kcal/mol.

HiPS. Nanocomposites incorporating HNT modified with 33% WB showed enhanced dispersion and reduced agglomeration. The observed improvement was attributed to the improved compatibility and stronger interactions due to the presence of a biocompatiblizing agent. It should be noted that there is a peak point beyond which addition of WB could lead to reduction in thermal resistance. The latter reduction is attributed to excess compatibilizer promoting degradation. Overall, wood-based biocrude was found to be a promising candidate as a modifier for the halloysite clay used in high-impact polystyrene. The results of this study can enable designers and manufacturers to properly incorporate biomodifiers such as those made from aspen wood to enhance the performance and sustainability of nanocomposites commonly used in construction and manufacturing.

## 4. MATERIALS AND METHODS

**4.1. Materials.** The high-impact polystyrene (HiPS) used in this study is Polystyrene 6540 from Total Petrochemicals. It has a melt flow index (MFI) of 12 g/10 min measured at 200 °C and a specific density of 1.04 g/cm$^3$. Unmodified halloysite nanotubes (HNTs) were acquired from Naturalnano Inc. The wood-derived biocrude (WB) was obtained through glycerol-assisted aspen wood liquefaction as reported elsewhere.[36] The WB was produced at 400 °C, 300 bars, in a continuous reactor with a residence time of approximately 15 min. Wood and



DOI: 10.1021/acsomega.9b02871
ACS Omega 2019, 4, 19934−19943

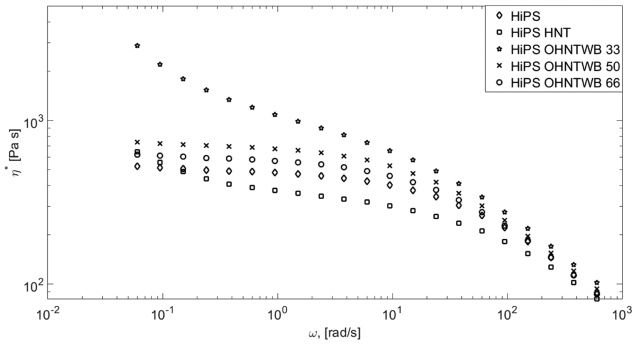


**Figure 6.** Complex viscosity versus angular frequency for average values of the HiPS nanocomposites.

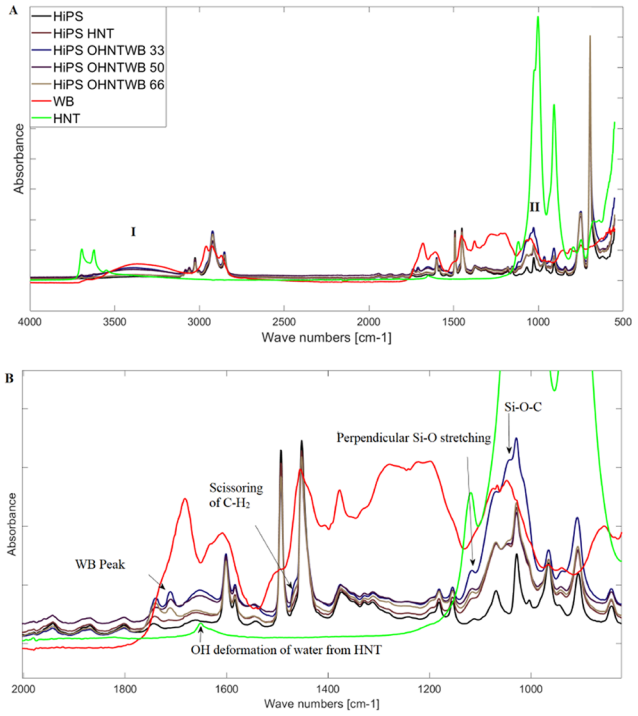


**Figure 8.** FTIR analysis of HiPS nanocomposites in the (A) 500–4000 $cm^{-1}$ range and (B) 800–2000 $cm^{-1}$ range.

glycerol were processed in a 50/50 mass ratio with a potassium carbonate catalyst. After processing, the biocrude and aqueous phases were separated gravimetrically and fractionated. The heavy residue is referred to as WB in this study. More information about the fractional distillation and chemical characterization of WB can be found in ref.[25]

**4.2. Preparation of Nanocomposites and Samples.** *4.2.1. Organic Surface Modification of HNT with WB.* Three batches of modified nanoclay with different WB concentrations were prepared. For each batch, a specified amount of HNT and WB was mixed in a 1:1 water/ethanol suspension. For each gram of HNT, 50 mL of deionized water was added to the clay and mixed by magnetic stirring for 25 min at 80 °C; the suspension was left to settle for approximately 24 h. The mixture was reheated for 5 min and mixed with a second solution of 10 mL of ethanol per gram of WB for 15 min. After

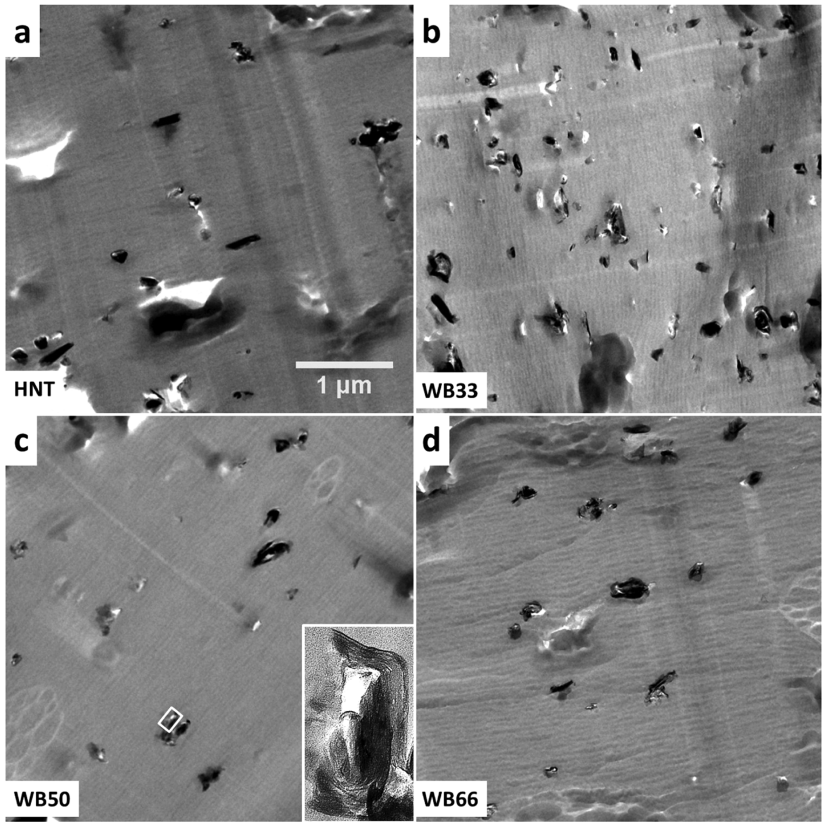


**Figure 7.** Transmission electron microscopy (TEM) images of thin sections of HiPS nanocomposites with (a) pure HNT, (b) OHNTWB 33, (c) OHNTWB 50, and (d) OHNTWB 66. All images have the same magnification. The inset in (c) is 125 nm wide and shows a magnified image of a sectioned nanotube.



DOI: 10.1021/acsomega.9b02871
*ACS Omega* 2019, 4, 19934–19943

Table 5. TG Analysis of the HiPS Nanocomposites after Four Extrusions

| | temperature range <600 °C | | residual mass at 600 °C | |
|---|---|---|---|---|
| | onset temperature [°C] | mass loss [%] | $R_{600}$ [%] | average temperature at maximum decomposition [°C] |
| HiPS | 409.9 | 100 | 0.0 | 428.9 |
| HiPS HNT | 411.9 ± 0.8 | 96.2 ± 0.1 | 3.8 ± 0.1 | 435.5 ± 0.5 |
| HiPS OHNTWB 33 | 414.3 ± 1.4 | 93.2 ± 0.9 | 6.8 ± 0.9 | 435.0 ± 0.8 |
| HiPS OHNTWB 50 | 415.6 ± 0.9 | 95.4 ± 0.2 | 4.6 ± 0.2 | 436.9 ± 0.6 |
| HiPS OHNTWB 66 | 415.6 ± 0.9 | 95.8 ± 0.1 | 4.2 ± 0.1 | 435.9 ± 0.5 |

mixing, sonication was performed with an ultrasonic horn for 2 min; the mixture was again left to settle for 24 h. All mixtures were then centrifuged for 60 min at 5000 rpm, and the sediment-modified nanoclay was collected and dried at room temperature. The collected modified nanoclays were ground by hand into fine powders for further processing and characterization. The weights of HNT and WB in each of the three batches are shown in Table 6.

Table 6. Weights of HNT and WB Compounds in Each Batch

| sample | wt of HNT | wt of WB |
|---|---|---|
| HNT | 100 | 0 |
| OHNTWB 33 | 66.66 | 33.33 |
| OHNTWB 50 | 50 | 50 |
| OHNTWB 66 | 33.33 | 66.66 |

*4.2.2. Preparation of OHNT/HiPS Nanocomposites.* The HiPS nanocomposites were processed via melt blending and compounding to obtain a masterbatch with a high concentration of modified nanoclay. The compounding was performed using an MC 15 Micro compounder from Xplore at 230 °C and a speed of 200 rpm, with a residence time of 180 s. This was followed by dilution using an extrusion process to a 5% filler concentration. The extrusion process was done with a Prism Euro-lab 16 twin-screw extruder from Thermo Scientific at 230 °C. This was followed by an injection molding to produce samples for characterization. The injection molding was done using a MiniJet Pro Piston Injection Molding System from HAAKR at 230 °C and 600 bars for 20 s. The postpressure was applied for 20 s at 600 bars with a tensile bar mold (ISO 527-2-5A) at 30 °C.

**4.3. Characterization Techniques.** *4.3.1. Rheological Properties.* The measurements were conducted to study potential interactions between the modified nanoclays and HiPS polymer, using a Paar Physica MCR 500 rheometer. A cone-and-plate configuration with a 25 mm diameter 2° cone and a gap of 0.105 mm was used for the measurements. The temperature setting was 230 °C for HiPS, and the measurements were performed in a frequency range of 600−0.06 rad/s using a 5% strain. The material was placed on the plate and left to melt for 180 s, after which the gap was set, and the system was left for 300 s to reach thermal equilibrium. All measurements were performed with three repetitions, and the average value for each material is reported.

*4.3.2. X-ray Diffraction (XRD).* XRD measurements to investigate the crystalline structures and properties of the nanoclays and nanocomposites were performed using an Empyrean diffractometer from PANalytical with a Cu K$\alpha$ radiation running at 45 kV and 40 mA.

*4.3.3. Transmission Electron Microscopy (TEM).* The TEM analysis was done using a Zeiss Libra 120 transmission electron microscope operating at 120 kV. To prepare samples, an RMC Boeckeler PT-PC PowerTome ultramicrotome was used to cut sections roughly 80−100 nm thick of the HiPS nanocomposites for TEM imaging. The sections were picked up using 200-mesh copper TEM grids and coated with 8 nm of carbon using a Leica EM ACE200 coating system.

*4.3.4. Attenuated Total Reflectance Fourier Transform Infrared (ATR-FTIR) Spectroscopy.* To assess the surface modification of the nanoclay and the interactions between the nanoclays and the HiPS, the functional groups were determined using a PerkinElmer Spectrum One spectrometer. A zinc selenide crystal was used in absorbance mode with a resolution of 4 $cm^{-1}$ and four scans per measurement in the 500−4000 $cm^{-1}$ range.

*4.3.5. Dynamic Light Scattering (DLS).* The average $\zeta$-potential and particle sizes of the pure and modified nanoclays were determined using a Malvern Zetasizer Nano ZS DLS. For each sample, 0.1 mg of clay was diluted in 15 mL of ethanol and then ultrasonicated for 20 min. The suspension was filled into the drip cell, and the analyses were conducted at room temperature.

*4.3.6. Thermogravimetric Analysis (TGA).* Thermal properties were determined using a Discovery TGA from TA Instruments, using platinum pans in a nitrogen atmosphere with a continuous flow of 10 mL/min. The temperature range was 40−1000 °C for the modified nanoclays and 40−600 °C for the nanocomposite, with a heating rate of 10 °C/min.

**4.4. Compatibility Studies.** The Yamamoto-Molecular Break (Y-MB) method was used to determine the Hansen solubility parameters (HSPs) of WB compounds using the HSPiP software. The HSP consists of three different parameters: dispersive ($\delta D$), polar ($\delta P$), and hydrogen bond ($\delta H$) cohesive forces. The compatibility between two materials can be assessed based on the relative energy difference (RED) given in eq 1, where a RED value greater than 1 indicates compatibility.

$$\mathrm{RED} = \frac{R_a}{R_o} \tag{1}$$

where the Hansen distance ($R_a$) between the compounds of WB and the polymer is calculated with eq 2.

$$R_a^2 = 4(\Delta\delta D_{12})^2 + (\Delta\delta P_{12})^2 + (\Delta\delta H_{12})^2 \tag{2}$$

where $\Delta\delta X_{12}$ is the difference between the individual HSP values of the HiPS and the WB compounds.

The interaction radius of the polymer ($R_o$) was set to 12.7, based on a theoretical generalization of polystyrene.

A secondary way to visualize compatibility is to calculate the fractional HSP ($f_{\delta X}$) of the compounds and plot them in a ternary diagram (Teas chart). The fractional HSP can be calculated with the following three equations.



DOI: 10.1021/acsomega.9b02871
ACS Omega 2019, 4, 19934−19943

$$f_{\delta D} = \frac{\delta D}{\delta D + \delta P + \delta H} f_{\delta P} = \frac{\delta P}{\delta D + \delta P + \delta H} f_{\delta H} = \frac{\delta H}{\delta D + \delta P + \delta H}$$

**4.5. Computational Methods.** Geometries of the monomers and all interacting constituents were fully optimized using the DMol$^3$ module[37,38] of the Accelrys Materials Studio program package (version 6.0). At the generalized gradient approximation (GGA) level, the Perdew–Burke–Ernzerhof (PBE) functional,[39] Grimme's dispersion corrections,[40] and double-numerical polarized (DNP) basis set were used for the optimization process.

The extended transition state–natural orbital of chemical valence (ETS-NOCV) approach, implemented in the Amsterdam density functional (ADF),[41] was subsequently performed on the molecules optimized in the previous step.

In the ETS-NOCV technique, the total binding energy is further decomposed into its chemically meaningful energy components, shown in eq 3.

$$\Delta E_{\text{bind}} = \Delta E_{\text{elstat}} + \Delta E_{\text{Pauli}} + \Delta E_{\text{orb}} + \Delta E_{\text{disp}} \quad (3)$$

where $E_{\text{elstat}}$ is the electrostatic interaction, $E_{\text{Pauli}}$ is the Pauli repulsion, and $E_{\text{orb}}$ is the dispersion interaction.

All ETS-NOCV calculations were performed at the dispersion-corrected PBE level including all-electron contracted double zeta valence plus polarization (DZP) function basis sets, the PBE-D3/DZP level.

## ■ ASSOCIATED CONTENT

### Supporting Information

The Supporting Information is available free of charge on the ACS Publications website at DOI: 10.1021/acsomega.9b02871.

Photographs and TEM images as well as Hansen solubility analysis and results; HSPs of samples of LDPE and PS and the chemical compounds; and TEM images of nanotube aggregates in the HiPS nanocomposites (PDF)

## ■ AUTHOR INFORMATION


### Corresponding Author

*E-mail: efini@asu.edu. Phone: 480-965-4273.

### ORCID

Masoumeh Mousavi: 0000-0003-4750-8154

Elham H. Fini: 0000-0002-3658-0006


### Notes

The authors declare no competing financial interest.

## ■ ACKNOWLEDGMENTS

The authors appreciate the support of the U.S. National Science Foundation (award numbers 1928807 and 1935723), Arizona State University, and Aalborg University of Denmark. The authors acknowledge the support of the Department of Energy Technology at Aalborg University for providing the wood-based biocrude. The content of this paper reflects the view of the authors, who are responsible for the facts and the accuracy of the data presented.

## ■ REFERENCES


(1) Bergaya, F.; Lagaly, G. General introduction: clays, clay minerals, and clay science. *Dev. Clay Sci.* **2006**, *1*, 1–18.

(2) Barrientos-Ramírez, S.; de Oca-Ramírez, G. M.; Ramos-Fernández, E.; Sepúlveda-Escribano, A.; Pastor-Blas, M.; González-Montiel, A. Surface modification of natural halloysite clay nanotubes with aminosilanes. Application as catalyst supports in the atom transfer radical polymerization of methyl methacrylate. *Appl. Catal., A* **2011**, *406*, 22–33.

(3) Joussein, E.; Petit, S.; Churchman, J.; Theng, B.; Righi, D.; Delvaux, B. Halloysite clay minerals–a review. *Clay Miner.* **2005**, *40*, 383–426.

(4) Carli, L. N.; Crespo, J. S.; Mauler, R. S. PHBV nanocomposites based on organomodified montmorillonite and halloysite: the effect of clay type on the morphology and thermal and mechanical properties. *Composites, Part A* **2011**, *42*, 1601–1608.

(5) Gorrasi, G. Dispersion of halloysite loaded with natural antimicrobials into pectins: Characterization and controlled release analysis. *Carbohydr. Polym.* **2015**, *127*, 47–53.

(6) Yuan, P.; Tan, D.; Annabi-Bergaya, F. Properties and applications of halloysite nanotubes: recent research advances and future prospects. *Appl. Clay Sci.* **2015**, *112–113*, 75–93.

(7) Liu, M.; Guo, B.; Du, M.; Cai, X.; Jia, D. Properties of halloysite nanotube–epoxy resin hybrids and the interfacial reactions in the systems. *Nanotechnology* **2007**, *18*, No. 455703.

(8) Vuluga, Z.; Corobea, M. C.; Elizetxea, C.; Ordonez, M.; Ghiurea, M.; Raditoiu, V.; Nicolae, C. A.; Florea, D.; Iorga, M.; Somoghi, R.; Trica, B. Morphological and Tribological Properties of PMMA/Halloysite Nanocomposites. *Polymers* **2018**, *10*, 816.

(9) Zhang, J.; Wang, X.; Lu, L.; Li, D.; Yang, X. Preparation and performance of high-impact polystyrene (HIPS)/nano-TiO2 nanocomposites. *J. Appl. Polym. Sci.* **2003**, *87*, 381–385.

(10) Arráez, F. J.; Arnal, M. L.; Müller, A. J. Thermal degradation of high-impact polystyrene with pro-oxidant additives. *Polym. Bull.* **2019**, *76*, 1489–1515.

(11) Carraher, C. E., Jr. *Giant Molecules: Essential Materials for Everyday Living and Problem Solving*, 2nd ed.; John Wiley and Sons, 2003; p 261.

(12) Lin, Y.; Ng, K. M.; Chan, C.-M.; Sun, G.; Wu, J. High-impact polystyrene/halloysite nanocomposites prepared by emulsion polymerization using sodium dodecyl sulfate as surfactant. *J. Colloid Interface Sci.* **2011**, *358*, 423–429.

(13) Rawtani, D.; Agrawal, Y. Multifarious applications of halloysite nanotubes: a review. *Rev. Adv. Mater. Sci.* **2012**, *30*, 282–295.

(14) Yuan, P.; Southon, P. D.; Liu, Z.; Green, M. E.; Hook, J. M.; Antill, S. J.; Kepert, C. J. Functionalization of halloysite clay nanotubes by grafting with γ-aminopropyltriethoxysilane. *J. Phys. Chem. C* **2008**, *112*, 15742–15751.

(15) Jana, S.; Kondakova, A. V.; Shevchenko, S. N.; Sheval, E. V.; Gonchar, K. A.; Timoshenko, V. Y.; Vasiliev, A. N. Halloysite nanotubes with immobilized silver nanoparticles for anti-bacterial application. *Colloids Surf., B* **2017**, *151*, 249–254.

(16) Pedrazzoli, D.; Pegoretti, A.; Thomann, R.; Kristof, J.; Karger-Kocsis, J. Toughening linear low-density polyethylene with halloysite nanotubes. *Polym. Compos.* **2015**, *36*, 869–883.

(17) Cavallaro, G.; Chiappisi, L.; Pasbakhsh, P.; Gradzielski, M.; Lazzara, G. A structural comparison of halloysite nanotubes of different origin by Small-Angle Neutron Scattering (SANS) and Electric Birefringence. *Appl. Clay Sci.* **2018**, *160*, 71–80.

(18) Bertolino, V.; Cavallaro, G.; Lazzara, G.; Milioto, S.; Parisi, F. Halloysite nanotubes sandwiched between chitosan layers: Novel bionanocomposites with multilayer structures. *New J. Chem.* **2018**, *42*, 8384–8390.

(19) Jia, Z.; Luo, Y.; Guo, B.; Yang, B.; Du, M.; Jia, D. Reinforcing and flame-retardant effects of halloysite nanotubes on LLDPE. *Polym.-Plast. Technol. Eng.* **2009**, *48*, 607–613.

(20) Khunova, V.; Kristóf, J.; Kelnar, I.; Dybal, J. The effect of halloysite modification combined with in situ matrix modifications on




DOI: 10.1021/acsomega.9b02871
*ACS Omega* 2019, 4, 19934–19943

the structure and properties of polypropylene/halloysite nanocomposites. *eXPRESS Polym. Lett.* **2013**, *7*, 471−479.
(21) Szczepanik, B.; Słomkiewicz, P.; Garnuszek, M.; Czech, K.; Banaś, D.; Kubala-Kukuś, A.; Stabrawa, I. The effect of chemical modification on the physico-chemical characteristics of halloysite: FTIR, XRF, and XRD studies. *J. Mol. Struct.* **2015**, *1084*, 16−22.
(22) Gaaz, T. S.; Sulong, A. B.; Kadhum, A. A. H.; Al-Amiery, A. A.; Nassir, M. H.; Jaaz, A. H. The impact of halloysite on the thermomechanical properties of polymer composites. *Molecules* **2017**, *22*, 838.
(23) Liu, M.; Zhang, Y.; Zhou, C. Nanocomposites of halloysite and polylactide. *Appl. Clay Sci.* **2013**, *75*−*76*, 52−59.
(24) Hansen, C. M. *Hansen Solubility Parameters: A User's Handbook*; CRC Press, 2007.
(25) Pedersen, T.; Jensen, C.; Sandström, L.; Rosendahl, L. Full characterization of compounds obtained from fractional distillation and upgrading of a HTL biocrude. *Appl. Energy* **2017**, *202*, 408−419.
(26) Cimmino, S.; Di Pace, E.; Martuscelli, E.; Silvestre, C. Syndiotactic Polystyrene: Crystallization and Melting Behaviour. *Polymer* **1991**, *32*, 1080−1083.
(27) Fini, E. H.; Høgsaa, B.; Christiansen, J. dC.; Sanporean, C.-G.; Jensen, E. A.; Mousavi, M.; Pahlavan, F. Multiscale Investigation of a Bioresidue as a Novel Intercalant for Sodium Montmorillonite. *J. Phys. Chem. C* **2017**, *121*, 1794−1802.
(28) Høgsaa, B.; Fini, E. H.; Christiansen, J. dC.; Hung, A. M.; Mousavi, M.; Jensen, E. A.; Pahlavan, F.; Pedersen, T. H.; Sanporean, C.-G. A Novel Bio-Residue to Compatibilize Sodium Montmorillonite and Linear Low Density Polyethylene. *Ind. Eng. Chem. Res.* **2018**, *57*, 1213−1224.
(29) Lertwimolnun, W.; Vergnes, B. Influence of compatibilizer and processing conditions on the dispersion of nanoclay in a polypropylene matrix. *Polymer* **2005**, *46*, 3462−3471.
(30) Lertwimolnun, W.; Vergnes, B. Influence of screw profile and extrusion conditions on the microstructure of polypropylene/organoclay nanocomposites. *Polym. Eng. Sci.* **2007**, *47*, 2100−2109.
(31) Mackay, M.; Dao, T.; Tuteja, A.; Ho, D.; Van Horn, B.; Kim, H.; Hawker, C. Nanoscale effects leading to non-Einstein-like decrease in viscosity. *Nat. Mater.* **2003**, *2*, 762−766.
(32) Dörr, A.; Sadiki, A.; Mehdizadeh, A. A discrete model for the apparent viscosity of polydisperse suspensions including maximum packing fraction. *J. Rheol.* **2013**, *57*, 743−765.
(33) Joo, Y.; Jeon, Y.; Lee, S. U.; Sim, J. H.; Ryu, J.; Lee, S.; Lee, H.; Sohn, D. Aggregation and stabilization of carboxylic acid functionalized halloysite nanotubes (HNT-COOH). *J. Phys. Chem. C* **2012**, *116*, 18230−18235.
(34) Meera, K.; Yang, C. S.; Choi, C. K. Bonding structure and electrical properties of SiOC (-H) films deposited with a methyltrimethoxysilane precursor by using inductively coupled plasma chemical vapor deposition. *J. Korean Phys. Soc.* **2006**, *48*, 1713−1718.
(35) Tham, W. L.; Poh, B. T.; Ishak, Z. A. M.; Chow, W. S. Thermal behaviors and mechanical properties of halloysite nanotube-reinforced poly (lactic acid) nanocomposites. *J. Therm. Anal. Calorim.* **2014**, *118*, 1639−1647.
(36) Pedersen, T. H.; Grigoras, I. F.; Hoffmann, J.; Toor, S. S.; Daraban, I. M.; Jensen, C. U.; Iversen, S. B.; Madsen, R. B.; Glasius, M.; Arturi, K. R.; et al. Continuous hydrothermal co-liquefaction of aspen wood and glycerol with water phase recirculation. *Appl. Energy* **2016**, *162*, 1034−1041.
(37) Delley, B. An all-electron numerical method for solving the local density functional for polyatomic molecules. *J. Chem. Phys.* **1990**, *92*, 508−517.
(38) Delley, B. From molecules to solids with the DMol3 approach. *J. Chem. Phys.* **2000**, *113*, 7756−7764.
(39) Perdew, J. P.; Burke, K.; Ernzerhof, M. Generalized gradient approximation made simple. *Phys. Rev. Lett.* **1996**, *77*, 3865.
(40) Grimme, S. Density functional theory with London dispersion corrections. *Wiley Interdiscip. Rev.: Comput. Mol. Sci.* **2011**, *1*, 211−228.
(41) Mitoraj, M. P.; Michalak, A.; Ziegler, T. A combined charge and energy decomposition scheme for bond analysis. *J. Chem. Theory Comput.* **2009**, *5*, 962−975.



DOI: 10.1021/acsomega.9b02871
*ACS Omega* 2019, 4, 19934−19943